Assessing Snow Albedo Feedback in Simulated Climate Change

Xin Qu and Alex Hall

Department of Atmospheric and Oceanic Sciences

University of California, Los Angeles

Los Angeles, California

corresponding author address:

Xin Qu

Department of Atmospheric and Oceanic Sciences

University of California, Los Angeles

Los Angeles, CA 90095

e-mail: xinqu@atmos.ucla.edu

For JCLI CCSM Special Issue

Abstract

According to classic climate sensitivity framework, we estimated two controlling aspects of snow albedo feedback over extratropical north America and Eurasia land areas based on the scenario runs of the current versions of two state-of-the-art climate models, GFDL CM2.0 and NCAR CCSM3.0: (1) the change in surface albedo induced by a unit temperature change and (2) the variation in planetary albedo with surface albedo. Although the snow albedo reduction from the current springtime climate to the climate of the end of the 21st century in the simulations is smaller in CCSM3.0 (3-4%) than CM2.0 (5-6%), the snow albedo reductions normalized by the local surface air temperature increases agree nearly perfectly in the two simulations in both continents. The snow albedo reduction is smaller in CCSM3.0 because the overall warming is smaller in this model, rather than because surface albedo is less sensitive to the temperature increase.

The second aspect, the impact of these snow albedo anomalies on top-of-the-atmosphere solar fluxes, is potentially a major source of error in the simulations of snow albedo feedback because clouds attenuate snow albedo anomalies as they are mirrored in planetary albedo anomalies, and errors in cloud fields could therefore result in errors in net incoming solar radiation changes. Here we develop a method to measure the simulated dependence of planetary albedo on snow albedo. We find that in both models, snow albedo anomalies result in planetary albedo anomalies one half as large, in spite of the two models having differences in mean cloud fields on the order of 20% in snow-covered regions. Moreover, when we apply the same method to the satellite-based ISCCP data set, we find agreement in this quantity with the simulations in spite of further disagreements between ISCCP and simulated cloud fields in snow-covered regions. This suggests errors in cloud fields do not result in significant error in simulation of this aspect of snow albedo feedback, enhancing our confidence in the climate

models.

Our study shows both factors governing the strength of snow albedo feedback simulated in CM2.0 are about the same as those simulated in CCSM3.0, thus implying the snow albedo feedback in the two models have about the same strength, being about 2.5 W/(m^{2}K) and 2.1 W/(m^{2}K) over extratropical North America and Eurasia land areas respectively. This may be an indication of convergence in simulations of snow albedo feedback in the new versions of climate models, although ensemble runs of the two models and more models need to be included in this comparison study. These analyses are currently underway.

1. Introduction

When the climate becomes warmer in climate change simulations with coupled land-ocean-atmosphere models, snow over the northern hemisphere (NH) extratropics retreats, and is replaced by land surface that is much less reflective of solar radiation. The additional absorbed solar radiation results in more warming (Cubasch et al. 2001; Holland and Bitz 2003). This positive climate feedback, the so-called snow albedo feedback, accounts for about half of the additional net incoming solar radiation associated with the NH sea ice and snow retreat in equilibrium climate change simulations (Hall 2004).

The satellite record also supports the idea that snow albedo feedback acts as a positive feedback. By correlating ERBE top-of-the-atmosphere short-wave fluxes and satellite-observed snow extent in the NH extratropics, Groisman et al. (1994a, b) pointed out that a large portion of the NH warming for the last two decades of the 20th century can be attributed to snow albedo feedback. Despite the consensus on the

sign of the feedback, the strength of the feedback seen in climate change simulations differs significantly (Cess et al. 1991; Randall et al. 1994; Cubasch et al. 2001; Holland and Bitz 2003). This is probably because physical aspects of snow albedo feedback are represented differently in climate models and also because this feedback interacts differently with other climate feedbacks in climate models. These differences become a source of divergence in simulated greenhouse gas induced climate change (Cubasch et al. 2001; Holland and Bitz 2003).

The main goal of this paper is to examine the strength of snow albedo feedback in simulated climate change in isolation from other climate feedbacks. Where possible, we also aim to compare aspects of simulated snow albedo feedback with the available satellite record. The simulations are done with new versions of two state-of-the-art climate models: Geophysical Fluid Dynamics Laboratory (GFDL) CM2.0 and National Center for Atmospheric Research (NCAR) CCSM3.0. The simulated current climate and the climate of the end of the 21st century are each extracted from history and future scenario runs of the two models. The strength of snow albedo feedback quantified from these simulations is probably close to that in equilibrium CO_2 doubling experiments with atmosphere-mixed-layer-ocean models (Hall 2004). Our study focuses on springtime (MAM). The reason for this is that over half the increase in net incoming solar radiation associated with snow retreat occurs during this season in climate change simulations (Hall 2004), as both snow extent and incoming solar radiation are relatively large. However, the methods we develop here can be easily extended to other seasons, and other simulations.

According to the classic climate sensitivity framework (e.g., Cess and Potter 1988),

the strength of snow albedo feedback in climate change can be quantified by the variation in net incoming shortwave radiation (Q) with surface air temperature (T_s) due to changes in surface albedo (α_s), $(\partial Q/\partial T_s)_{SAF}$:

$$(\frac{\partial Q}{\partial T_s})_{SAF} = \frac{\Delta \alpha_s}{\Delta T_s} \cdot \frac{\partial Q}{\partial \alpha_s} \tag{1}$$

where the subscript SAF is used to emphasize that the partial derivative refers only to changes in solar radiation with surface temperature that occur due to changes in the snow pack, rather than changes in cloudiness or other factors that could affect solar radiation. According to eq. (1), snow albedo feedback is the product of two terms, one representing the change in surface albedo induced by a unit temperature change ($\Delta \alpha_s/\Delta T_s$), and another representing the dependence of net incoming solar radiation on surface albedo ($\partial Q/\partial \alpha_s$).

In this study, we focus mainly on the second term, $\partial Q/\partial \alpha_s$. It can be rewritten as follows:

$$\frac{\partial Q}{\partial \alpha_s} = -I_t \cdot \frac{\partial \alpha_p}{\partial \alpha_s} \tag{2}$$

where I_t is the incoming solar radiation at the top of atmosphere (TOA), which we take to be a constant, and $\partial \alpha_p/\partial \alpha_s$ is the variation in planetary albedo with snow albedo. It represents the attenuation effect of the atmosphere on snow albedo anomalies. The atmosphere attenuates the surface's contribution to planetary albedo fluctuations in two ways: First, incoming solar photons at the TOA are partly absorbed and reflected back to space by the atmosphere, reducing the number reaching the surface; Second, solar photons initially reflected by the surface are partly absorbed and reflected back to

the surface by the atmosphere, reducing the number reaching the TOA. Obviously the more the atmosphere absorbs and scatters solar radiation due to factors such as water vapor concentration and cloudiness, the greater the atmospheric attenuation of snow albedo.

Because planetary albedo changes ($\Delta\alpha_p$) from the current climate to the climate of the end of the 21st century are given in simulations, the ratio, $\Delta\alpha_p/\Delta\alpha_s$, rather than $\partial\alpha_p/\partial\alpha_s$ has been used to quantify the strength of this aspect of snow albedo feedback (Cess 1991 et al. 1991; Randal et al. 1994). However, simulated planetary albedo changes in snow-covered regions can also stem from changes in cloud fields, such as cloud cover and cloud optical thickness, and thus values of $\partial\alpha_p/\partial\alpha_s$ are generally not equal to $\Delta\alpha_p/\Delta\alpha_s$. Therefore, this approach does not allow us to separate snow albedo feedback from cloud feedback. As a result, it introduces model divergence associated with cloud feedback into snow albedo feedback. This is probably a significant source of the divergence in previous estimates of simulated snow albedo feedback. Moreover, because values of $\partial\alpha_p/\partial\alpha_s$ are partly determined by mean cloud fields, and also because simulated mean cloud fields differ among climate models, values of $\partial\alpha_p/\partial\alpha_s$ probably vary with from model to model as well. This may be another source of the divergence in the strength of simulated snow albedo feedback. Finally, because mean cloud fields likely vary in climate change, values of $\partial\alpha_p/\partial\alpha_s$ probably also vary with time. This may make it difficult to use a single value to represent the strength of this aspect of snow albedo feedback in climate change.

Because intermodel variations in cloud fields as well as climate-change-induced variations in cloud within any particular simulation inevitably complicate efforts to quantify

$\partial\alpha_p/\partial\alpha_s$, we develop an analytical model of planetary albedo, where planetary albedo is represented as a function of known model variables, such as surface albedo, cloud cover and cloud optical thickness. We determine the cofficients of the terms relating these variables to planetary albedo empirically from model output. The advantage of such an analytical model is that calculation of a true partial derivative with respect to surface albedo is straightforward. This allows us to separate snow albedo feedback from cloud feedback; to examine whether differences in mean cloud fields among models and changes in mean cloud fields from the current climate to future warmer climate will modify values of $\partial\alpha_p/\partial\alpha_s$ significantly. Of course, our results rest upon the ability of our analytical model to capture simulated variations in planetary albedo given quantities such as surface albedo, cloud cover and cloud optical thickness. We find that it does remarkably well in this regard, and is therefore extremely useful for evaluating this aspect of snow albedo feedback. Moreover, we find we can apply the same model with a high degree of accuracy to International Satellite Cloud Climatology Project (ISCCP) data from 1984 to 2000. This facilitates the use of satellite data to assess the accuracy of the simulations.

Using the analytical model, we compare values of $\partial\alpha_p/\partial\alpha_s$ between current and future climate in both simulations to assess the effect of changes in cloud fields on this quantity. We also compare values of $\partial\alpha_p/\partial\alpha_s$ between the two models to assess the effect of differences in mean cloud fields between the two models on values of $\partial\alpha_p/\partial\alpha_s$. Finally, if values of $\partial\alpha_p/\partial\alpha_s$ in simulated current climate in GFDL CM2.0 and NCAR CCSM3.0 are very different from those seen in observations, we would expect large errors in simulated snow albedo feedback. To examine whether this is the case, we compare

this quantity in the models' current climate to that seen in ISCCP. Our study is part of an overall effort to measure the strength of snow albeo feedback in climate simulations and use available observations to constrain the models. Our strategy is to break down the feedback into its two consitutent components and evaluate each independently. Though the size of snow albedo anomalies induced by the temperature anomalies of transient climate change ($\Delta\alpha_s/\Delta T_s$ in eq. (1)) is also an important aspect of snow albedo feedback, a detailed study of this factor in climate models and observations is beyond the scope of the present study, though we touch on it briefly.

This study is presented as follows: A brief description of NCAR CCSM3.0, GFDL CM2.0 and ISCCP data sets is given in Section 2, followed by a discussion of simulated changes in springtime surface albedo, cloud cover, logarithm of cloud optical thickness and planetary albedo from the current climate to the climate of the end of the 21st century in NH extratropics in Section 3. An analytical model for planetary albedo is developed and validated against simulated and ISCCP data sets in Section 4. In Section 5, we use this model to obtain an expression for the partial derivative of planetary albedo with respect to surface albedo and assess it in the current and future climate based on simulated and ISCCP data sets. In Section 6, we use this model to assess the effect of surface-cloud interaction on the top-of-the-atmosphere albedo variations in climate change simulations. Summary and implications are found in Section 7.

2. Models and observations

2.1 NCAR CCSM3.0

A brief description of NCAR CCSM3.0 T85gx1v3 (referred to hereafter as CCSM3.0)

is given here. More details can be found in Collins et al. (2004), Oleson et al. (2004), Smith and Gent (2004) and Briegleb et al. (2004). It consists of general circulation models of the atmosphere and ocean, a land surface model and a sea-ice model, linked by a coupler. The atmospheric component, the Community Atmospheric Model (CAM3.0), is similar to previous versions of the Community Climate Model, but the cloud scheme now uses a prognostic liquid and ice water formation. T85 version has a horizontal resolution of approximately 1.4^0 latitude by 1.4^0 longitude and 26 vertical finite difference levels. The land surface component, the Community Land Model (CLM3.0), provides a simplified treatment of surface processes responsible for land-atmosphere exchange of heat, water and momentum. A canopy radiative transfer scheme is used to calculate surface albedo, accounting for the joint albedo effect of canopy and ground. It is controlled by the optical properties of both canopy and ground, including the exposed leaf and stem area indexes of canopy, plant functional type optical properties, the wetted fraction of canopy and ground albedo. Ground albedo is a weighted combination of soil and snow albedos by snow cover, which in turn is a function of snow depth. Snow albedo is parameterized as a function of solar zenith angle and snow age.

The oceanic component, CCSM POP, is an extension of the Parallel Ocean Program (POP) Version 1.4.3 from Los Alamos National Laboratory. It has 320×384 points horizontally and 40 ocean levels vertically. The sea-ice component, the Community Sea-Ice Model (CSIM5.0), is a dynamic-thermodynamic model that includes a subgrid-scale ice thickness distribution, energy conserving thermodynamics, and elastic-viscous-plastic dynamics.

The CCSM3.0 cloud and flux data sets corresponding to the 1984 to 1999 period

are extracted from the CCSM3.0 1870-present history run, b30.030c. The data sets corresponding to the year 2000 and the years from 2080 to 2096 are extracted from the CCSM3.0 future scenario (A1B) run, b30.040c.

2.2 GFDL CM2.0

Similar to CCSM3.0, the GFDL CM2.0 (referred to hereafter as CM2.0) consists of general circulation models of the atmosphere and ocean, a land surface model and a sea ice model. The atmosphere component, AM2, uses a new grid point dynamical core, a prognostic cloud scheme and a multi-species aerosol climatology (GFDL GAMDT 2004). It has a horizontal resolution of 2.5^0 longitude by 2^0 latitude and 24 vertical levels. The land component, LM2, is based on the Land Dynamics (LaD) model described by Milly and Shmakin (2002). It uses soil sensible and latent heat storage, groundwater storage and stomatal resistance. Surface albedo over snow-covered regions is parameterized as an average of snow-free surface albedo and snow albedo, which are weighted by snow cover. Snow cover is in turn a function of snow depth. Snow albedo is parameterized as a function of surface temperature. Note that this scheme does not explicitly include canopy effects in its calculation of surface albedo, as is the case with the CCSM3.0 scheme.

The model has full 3-dimensional dynamical ocean as well as a complex sea ice model; however, no official documentation of the ocean and sea ice components of CM2.0 is available when this article was composed.

The CM2.0 cloud and flux data sets correspondng to the 1984 to 2000 period are extracted from the CM2.0 20th century climate run, 20c3m. The data sets correspond-

ing to the 2080 to 2096 period are extracted from the CM2.0 future scenario (A1B) run, sresa1b.

2.3 ISCCP data sets

The ISCCP D-series cloud data sets used in this study are based on observations from a suite of operational weather satellites measuring the temporal and spatial distribution of visible (VIS wavelength $\approx 0.6\ \mu m$), near-infrared (NIR wavelength $\approx 3.7\ \mu m$) and infrared (IR wavelength $\approx 11\ \mu m$) radiation. These measurements are then employed to retrieve information about clouds, such as cloud cover, cloud optical thickness and cloud top pressure (Rossow and Schiffer 1991; Rossow and Garder 1993a,b; Rossow et al. 1993; Rossow and Schiffer 1999). Three changes have been made in the D-series datasets to enhance the accuracy of cloud detection over snow- and ice-covered surfaces (Rossow and Schiffer 1999): (1) most importantly, a new threshold test on 3.7 μm radiances was used, exploiting significantly greater contrast between cloudy and clear scenes over snow- and ice-covered surfaces at this frequency than at 0.6 μm; (2) at the high latitudes, the visible radiance threshold test was changed to a visible reflectance threshold test; (3) over snow and ice in the polar regions, both the VIS and IR thresholds were lowered. Together these improvements have been shown to increase significantly low-level cloud detection sensitivity over snow and ice and reduce the biases in cloud optical thickness of previous ISCCP C-series datasets in these regions.

Accompanying the ISCCP D-series cloud data sets are radiative flux data sets containing solar and infrared radiative fluxes at the TOA and surface for both clear-sky and full-sky situations. They are calculated by specifying the following information in

a radiative transfer model (Zhang et al. 2004): (1) atmospheric temperature and humidity profiles; (2) vertical profiles of various atmospheric gases, such as CO_2, O_3, O_2 and CH_4; (3) vertical aerosol profiles for the troposphere and stratosphere; (4) ISCCP D-series cloud datasets; (5) snow and ice cover data. All the data mentioned above are time-varying so that observed variations in radiative properties of the atmosphere and surface are reflected in the fluxes at the TOA and surface.

These data sets are provided on a global $2.5^0 \times 2.5^0$ grid and cover the period from 1984 to 2000.

3. Simulated reduction in planetary albedo over snow-covered regions

Fig 1 shows simulated changes in springtime surface albedo (α_s), cloud cover (c), logarithm of cloud optical thickness ($ln(\tau + 1)$) and planetary albedo (α_p) from the current climate to the climate of the end of the 21st century in NH extratropics. We show the logarithm of cloud optical thickness (τ) rather than τ itself to take account of the quasi-logarithmic dependence of cloud albedo on τ (Rossow et al. 1996). Because cloud liquid water path (c_{lwp}) and ice water path (c_{iwp}) rather τ are provided by the CM2.0 and CCSM3.0 data sets, a relation is used to convert c_{lwp} and c_{iwp} into τ:

$$\tau = \kappa_1 \cdot c_{lwp} + \kappa_2 \cdot c_{iwp} \tag{3}$$

where κ_1 and κ_2 are assumed to be 0.16 and 0.10, respectively, in accordance with those used by the ISCCP (Rossow et al. 1996). This facilitates the comparison between

ISCCP data sets and model data sets in the current climate in Sections 4 and 5.

As shown in Fig 1, surface albedo in the warmer climate in both CM2.0 and CCSM3.0 decreases in the high latitudes of North America and Eurasia, especially in northern Canada and western Russia. However, the decrease is much greater in CM2.0 than CCSM3.0. The surface albedo reductions averaged over extratropical North America and Eurasia in CM2.0 are about 5-6%, but are only about 3-4% in CCSM3.0 (see Fig 2). The smaller surface albedo reduction in CCSM3.0 is probably either because surface albedo is less sensitive to the change in surface air temperature or because the overall warming is smaller in the model. To clarify this, we calculate the increase in surface air temperature from the current to the future climate in CM2.0 and CCSM3.0. As shown in Table 1, the increase in surface air temperature (ΔT_s) over NH extratropical lands in CCSM3.0 is about 2/3 that of CM2.0. However, the ratio, $\Delta\alpha_s/\Delta T_s$ is about the same in the models. This implies the surface albedo reduction in CCSM3.0 is relatively small because the overall warming is smaller in this model, rather than because surface albedo is less sensitive to surface air temperature anomalies. This in turn, is due to the smaller strength of other climate feedbacks in CCSM3.0, mostly likely global cloud feedback.

Changes in cloud cover and cloud optical thickness simulated in CM2.0 and CCSM3.0 differ not only in amplitude, but also in sign. Cloud cover in CM2.0 decreases in the warmer climate nearly everywhere in North America and Eurasia, especially in the western United States and western Europe. This reduction averaged over extratropical North America and Eurasia is about 2% and 4% (see Fig 2). In contrast, cloud cover simulated in CCSM3.0 increases in the high latitudes of Eurasia and nearly ev-

erywhere in North America, especially in the United States, and decreases only in the middle latitudes of Eurasia. Cloud cover averaged over extratropical North America increases 2%, but decreases 1% over extratropical Eurasia (see Fig 2). The logarithm of cloud optical thickness in CM2.0 increases in the warmer climate nearly everywhere in North America and Eurasia. This increase averaged over extratropical North America and Eurasia is about 0.25 (see Fig 2), about one tenth of the mean springtime value (2.3). The logarithm of cloud optical thickness in CCSM3.0 increases in the high latitudes of Eurasia and nearly everywhere in North America, but decreases in the middle latitudes of Eurasia. This change averaged over extratropical North America is 0.1, and is slightly positive over extratropical Eurasia (Fig 2). The disparity in changes in cloud fields between the two models is consistent with the wide divergence in simulations of cloud feedback among current climate models. We are particularly concerned with this divergence because it complicates our ability to assess surface albedo feedback independently of cloud changes in snow-covered regions.

Planetary albedo in CM2.0 and CCSM3.0 decreases nearly everywhere in the high latitudes of North America and Eurasia, especially in regions with strong snow albedo reduction, such as northern Canada and western Russia. As shown in Fig 2, planetary albedo reduction averaged over extratropical North America and Eurasia in CM2.0 is about 3%, about half the albedo reduction at the surface. Planetary albedo reduction averaged over extratropical Eurasia in CCSM3.0 is about 1.8%, also about half the albedo signature at the surface. The planetary albedo reduction averaged over extratropical North America in CCSM3.0 is only about 1%, considerably less than that averaged over extratropical Eurasia, in spite of the fact that the surface albedo reduc-

tion over extratropical North America is slightly greater than that over extratropical Eurasia. One question we aim to answer is to what extent these relationships between surface albedo and planetary albedo are affected by the cloud changes seen in Fig 2.

4. An analytical model to understand planetary albedo

In the previous section, we showed that surface albedo, cloud cover and cloud optical thickness probably all contribute to the simulated planetary albedo change in the warmer climate. To isolate the surface contribution from that of cloud, we develop an analytical model governing planetary albedo, and validate it against simulated and satellite-based data sets. This model relates full-sky planetary albedo to known quantities, including clear-sky planetary albedo, cloud cover, cloud optical thickness and surface albedo. This allows us to generate an analytical expression for the variation in planetary albedo with surface albedo, a quantity representing the size of the attenuation effect of the atmosphere on the surface's contribution to planetary albedo fluctuations. We can then compare this quantity among models and satellite-based data sets, and use it to separate the surface and cloud contributions to planetary albedo reduction seen in Figs 1 and 2.

This model is derived as follows: Full-sky planetary albedo, α_p can be written as the weighted mean of clear-sky planetary albedo (α_p^{cr}) and cloudy-sky planetary albedo (α_p^{cd}):

$$\alpha_p = (1 - c) \cdot \alpha_p^{cr} + c \cdot \alpha_p^{cd} \tag{4}$$

In eq. (4), α_p^{cr} is given as follows:

$$\alpha_p^{cr} = \alpha_a^{cr} + T_a^{cr} \cdot \alpha_s \tag{5}$$

which is the sum of clear-sky atmospheric albedo to incoming solar radiation (α_a^{cr}), and a surface albedo component, which is the product of α_s and an effective clear-sky atmospheric transmissivity, T_a^{cr}. In eq. (4), α_p^{cd} is given as follows:

$$\alpha_p^{cd} = \alpha_a^{cd} + T_a^{cd} \cdot \alpha_s \tag{6}$$

which is the sum of cloudy sky atmospheric albedo to incoming solar radiation (α_a^{cd}), and a surface albedo component, which is the product of α_s and an effective cloudy sky atmospheric transmissivity, T_a^{cd}. We model the difference between clear and cloudy sky atmospheric albedo as being proportional to the logarithm of cloud optical thickness, thereby linking α_a^{cr} in eq. (5) and α_a^{cd} in eq. (6):

$$\alpha_a^{cd} = \alpha_a^{cr} + \varepsilon_1 \cdot ln(\tau + 1) \tag{7}$$

In eq. (7), ε_1 is the linear coefficient relating the logarithm of cloud optical thickness to the cloudy-sky atmospheric albedo. Similarly, we model the difference between clear and cloudy sky effective transmissivity as being proportional to the logarithm of cloud optical thickness, thereby linking T_a^{cr} in eq. (5) and T_a^{cd} in eq. (6):

$$T_a^{cd} = T_a^{cr} - \varepsilon_2 \cdot ln(\tau + 1) \tag{8}$$

where ε_2 is the linear coefficient relating the logarithm of cloud optical thickness to the effective cloudy-sky atmospheric transmissivity.

We plug eqs. (5)-(8) into (4), and rearrange it into

$$\alpha_p = \alpha_p^{cr} + c \cdot ln(\tau + 1) \cdot (\varepsilon_1 - \varepsilon_2 \cdot \alpha_s) \tag{9}$$

We can rewrite eq. (9) as follows:

$$\alpha_p - \alpha_p^{cr} = \varepsilon_1 \cdot c \cdot ln(\tau + 1) - \varepsilon_2 \cdot c \cdot ln(\tau + 1) \cdot \alpha_s \tag{10}$$

Because α_p, α_p^{cr}, c, $ln(\tau + 1)$ and α_s are given in the models and observations, values of two linear coefficients, ε_1 and ε_1, can be readily obtained by regressing $(\alpha_p - \alpha_p^{cr})$ onto $c \cdot ln(\tau + 1)$ and $c \cdot ln(\tau + 1) \cdot \alpha_s$.

Eq. (9) is our analytical model for planetary albedo. To test how well it captures planetary albedo and its temporal and spatial variability, we apply it to three data sets: ISCCP, CM2.0 and CCSM3.0 in the current climate. First, α_p, α_p^{cr}, c, $ln(\tau + 1)$ and α_s in March, April and May over 17 years were averaged to get a time-series of springtime-mean values at each location within extratropical North America and Eurasia. Then, the difference between full-sky and clear-sky planetary albedo, $(\alpha_p - \alpha_p^{cr})$ was regressed onto $c \cdot ln(\tau + 1)$ and $c \cdot ln(\tau + 1) \cdot \alpha_s$ to obtain values of ε_1 and ε_2. We perform the regression calculation based on concantenated time series of all locations within extratropical North America and Eurasia, so that we are attempting to capture both interannual and geographical variability in planetary albedo. This provides samples

large enough to achieve stable statistics, the size of samples being larger than 8000. We can then model interannual and geographical variations in planetary albedo from this analytical model by plugging in these values of ε_1 and ε_2, as well as values of c, τ, α_p^{cr} and α_s into eq. (9). Fig 3 shows the scatterplot of modeled planetary albedo against actual planetary albedo in the three data sets. They almost exactly follow a diagonal line, implying nearly perfect agreement. The correlation coefficient is very close to unity, as shown in the right-bottom corner of each scatterplot. Eq. (9) is also used to model planetary albedo in the future climate in CM2.0 and CCSM3.0 by plugging in the values of ε_1 and ε_2 obtained from the current climate, as well as values of c, τ, α_p^{cr} and α_s in the future climate. Fig 4 shows the scatterplot of modeled planetary albedo against actual planetary albedo in the two models. Similarly, they are nearly perfectly correlated. This implies eq. (9) captures the physical relationship seen in the models and ISCCP data set among planetary albedo, surface albedo and clouds extremely well.

To reveal physical insights behind eq. (9), we rearrange it:

$$\alpha_p = (\alpha_a^{cr} + \varepsilon_1 \cdot c \cdot ln(\tau + 1)) + (T_a^{cr} - \varepsilon_2 \cdot c \cdot ln(\tau + 1)) \cdot \alpha_s \tag{11}$$

The first term, $(\alpha_a^{cr} + \varepsilon_1 \cdot c \cdot ln(\tau + 1))$ in eq. (11) can be viewed as an effective full-sky atmospheric albedo. It is attributed partly to the clear-sky atmosphere (α_a^{cr}) and partly to clouds ($\varepsilon_1 \cdot c \cdot ln(\tau + 1)$). The second term, $(T_a^{cr} - \varepsilon_2 \cdot c \cdot ln(\tau + 1)) \cdot \alpha_s$ can be viewed as a surface albedo component of full-sky planetary albedo, which is the product of α_s and an effective full-sky atmospheric transmissivity ($T_a^{cr} - \varepsilon_2 \cdot c \cdot ln(\tau + 1)$). The latter is attributed partly to the clear-sky atmosphere (T_a^{cr}) and partly to clouds ($-\varepsilon_2 \cdot c \cdot ln(\tau +$

1)). The two terms involving clouds in eq. (11), $(\varepsilon_1 \cdot c \cdot ln(\tau+1))$ and $(-\varepsilon_2 \cdot c \cdot ln(\tau+1) \cdot \alpha_s)$ represent two effects on planetary albedo: (1) clouds increase planetary albedo through their own reflectivity; (2) clouds decrease the surface contribution to planetary albedo by reducing the effective full-sky atmospheric transmissivity. In both cases, the effect is proportional to the product of cloud cover and the logarithm of cloud optical thickness.

The advantage of eq. (11) is to allow us to assess contributions of clear-sky atmosphere, clouds and surface to planetary albedo and its variability separately in a relatively simple and analytical manner. It also facilitates the examination of surface-cloud interaction in terms of top-of-the-atmosphere short-wave radiation budget. These advantages are illustrated in detail in Sections 5 and 6.

5. Dependence of planetary albedo on surface albedo ($\partial\alpha_p/\partial\alpha_s$)

The partial derivative, $\partial\alpha_p/\partial\alpha_s$ represents the attenuation effect of the atmosphere on the surface's contribution to planetary albedo fluctuations. Its significance in modulating the surface-induced planetary albedo fluctuations can be illustrated through two extreme cases. In one case, the atmosphere is so opaque that none of the incoming solar photons at the TOA reach the surface. For this case, $\partial\alpha_p/\partial\alpha_s = 0$, and surface albedo fluctuations have no effect on net TOA solar fluxes. In the other case, the atmosphere is completely transparent to solar radiation, so that all the incoming photons at the TOA reach the surface and all the upwelling solar photons reflected by the surface make it to space. For this case, $\partial\alpha_p/\partial\alpha_s = 1$, and surface albedo fluctuations translate directly into planetary albedo fluctuations without any attenuation. Of course, values of $\partial\alpha_p/\partial\alpha_s$ for the real atmosphere are somewhere between these two extremes.

Eq. (11) is such a successful model for planetary albedo that we can use it to derive an expression for the partial derivative, $\partial\alpha_p/\partial\alpha_s$. Taking the partial derivative of eq. (11) with respect to surface albedo, we obtain an expression for $\partial\alpha_p/\partial\alpha_s$:

$$\partial\alpha_p/\partial\alpha_s = T_a^{cr} - \varepsilon_2 \cdot c \cdot ln(\tau + 1) \tag{12}$$

The right-hand side of eq. (12) represents the total attenuation effect of the atmosphere on the surface's contribution to planetary albedo fluctuation. This includes a contribution from the cloudless atmosphere, represented by T_a^{cr}, as well as a contribution from cloud, being proportional to the product of cloud cover and the logarithm of cloud optical thickness. Eq. (12) is useful because it is a true partial derivative providing the dependence of planetary albedo on surface albedo given key information about clouds. The direct effects of the changes in cloudiness on planetary albedo are not included in eq. (12), and so are not conflated with the effects of changes in surface albedo, as is the case if the dependence of planetary albedo on surface albedo is measured by simply regressing planetary albedo variations onto their counterparts at the surface. This points to the importance of our analytical model, eq. (11) in unraveling surface and cloud's contributions to planetary albedo variations in cryosphere regions. We will use eq. (12) to assess the values of $\partial\alpha_p/\partial\alpha_s$ in the current climate and future climate.

The quantities c and τ are given by the ISCCP and model data sets, while ε_2 is known from regression analysis relying on eq. (10). The unknown quantity on the right-hand side of eq. (12) is therefore the clear-sky effective atmospheric transmissivity, T_a^{cr}. Relying on eq. (5), we can obtain it by regressing clear-sky planetary albedo, α_p^{cr} onto

surface albedo, α_s. In analogy with Figs 3 and 4, we show a scatterplot of modeled clear-sky planetary albedo against the actual clear-sky planetary albedo in Figs 5 and 6 as a validation of this regression model. They follow a diagonal line almost exactly and the correlation coefficient, shown in the right-bottom corner of each scatterplot, is very close to unity, implying nearly perfect agreement. Fig 7 shows values of T_a^{cr} seen in ISCCP, CM2.0 and CCSM3.0 in North America and Eurasia. There is a good agreement in values of T_a^{cr} in the current climate among ISCCP, CM2.0 and CCSM3.0, and in the future climate between CM2.0 and CCSM3.0 in both continents, being about 0.7. This implies the clear-sky atmosphere attenuates snow albedo fluctuations so that their magnitude is reduced by about 30% as they are mirrored in planetary albedo variations.

According to Fig 7, there is also a good agreement in values of $\varepsilon_2 \cdot c \cdot ln(\tau + 1)$ in the current and future climate in both continents, all being about 1/3 as large as values of T_a^{cr}. Values of $\varepsilon_2 \cdot c \cdot ln(\tau + 1)$ are relatively small because values of ε_2, the regression coefficient relating cloud optical thickness to cloudy sky transmissivity are generally smaller than 0.2, as shown in Table 2. Because of this, differences in values of $\varepsilon_2 \cdot c \cdot ln(\tau + 1)$ in the current and future climate among the three data sets are generally smaller than 0.1, in spite of the fact that cloud fields differ somewhat in the current and future climate among the three data sets (see Table 2).

The mean values of $\partial\alpha_p/\partial\alpha_s$ seen in ISCCP, CM2.0 and CCSM3.0 in the current and future climate have general agreement, all being about 0.5 (Fig 7), implying the size of snow-induced planetary albedo fluctuations is about half the albedo signature at the surface. This agreement among the values of $\partial\alpha_p/\partial\alpha_s$ is because differences in

values of $\varepsilon_2 \cdot c \cdot ln(\tau + 1)$ are constrained due to the small values of ε_2, as discussed above. This is the case in spite of the disparity in cloud fields among ISCCP, CM2.0 and CCSM3.0, between North America and Eurasia within individual data sets, and within regions going from the present-day to future simulated climates. This demonstrates that disparities in the cloud fields larger than those seen in the ISCCP, CCSM3.0, or CM2.0 are required to generate appreciable divergence in values of $\partial\alpha_p/\partial\alpha_s$.

6. Surface-cloud interaction in transient climate change

Surface-cloud interaction complicates the attribution of planetary albedo reduction in transient climate change. As demonstrated in Section 4, there are two possible ways clouds can interact with the surface in terms of top-of-the-atmosphere short-wave radiation budget: (1) clouds amplify or diminish the planetary albedo reduction associated with surface albedo reduction in the future climate through their own reflectivity; (2) clouds amplify or diminish the planetary albedo reduction associated with surface albedo reduction in the future climate by changing the effective atmospheric transmissivity ($\partial\alpha_p/\partial\alpha_s$). Our analytical model, eq. (11) allows us to examine the two effects independently.

Based on this model, in the previous section we demonstrated that the second effect of clouds on planetary albedo is very small. In this section, we use it to examine whether clouds can modify significantly the planetary albedo reduction associated with surface albedo reduction in the future climate through the first effect.

Linearizing eq. (11), we can readily break down the planetary albedo reduction into

surface and cloud contributions as follows:

$$\Delta\alpha_p = \frac{\partial\alpha_p}{\partial\alpha_s} \cdot \Delta\alpha_s + \frac{\partial\alpha_p}{\partial c} \cdot \Delta c + \frac{\partial\alpha_p}{\partial ln(\tau+1)} \cdot \Delta ln(\tau+1) \tag{13}$$

where $\partial\alpha_p/\partial c$ and $\partial\alpha_p/\partial ln(\tau+1)$ represent planetary albedo variations with cloud cover and logarithm of cloud optical thickness, respectively. For the sake of interpretation, we normalize eq. (13) by surface albedo reduction ($\Delta\alpha_s$):

$$\frac{\Delta\alpha_p}{\Delta\alpha_s} = \frac{\partial\alpha_p}{\partial\alpha_s} + \frac{\partial\alpha_p}{\partial c} \cdot \frac{\Delta c}{\Delta\alpha_s} + \frac{\partial\alpha_p}{\partial ln(\tau+1)} \cdot \frac{\Delta ln(\tau+1)}{\Delta\alpha_s} \tag{14}$$

In eq. (14), we know $\Delta\alpha_s$, $\Delta\alpha_s$ and $\partial\alpha_p/\partial\alpha_s$ so we can easily solve for the cloud contribution (the last two terms on the right-side of eq. (14)). We show the normalized planetary albedo reduction, the surface contribution and cloud contribution in Fig 8.

A comparison of normalized planetary albedo reduction and the surface contribution in the top panel of Fig 8 reveals that nearly all the planetary albedo reduction seen in CM2.0 stems from the surface albedo reduction in both North America and Eurasia. This is mostly because the magnitudes of the cloud contributions are small and also because the positive contribution of cloud cover is compensated by a negative contribution of cloud optical thickness (see Figs 1 and 2). Likewise, clouds in CCSM3.0 do not contribute much to planetary albedo change in Eurasia. However, in North America, the increase in planetary albedo due to the increase in cloud cover and cloud optical thickness partly cancels the effect of the surface albedo reduction, so that the final planetary albedo reduction is only a third of what it would be if there were no

cloud feedback.

This demonstrates that cloud feedback can modify significantly short-wave radiation flux anomaly associated with surface albedo reduction in transient climate change. This also suggests the divergence of simulated cloud feedback is most likely a major reason values of $\Delta\alpha_p/\Delta\alpha_s$ diverge significantly among climate models in the previous estimates of snow albedo feedback.

7. Summary and Implications

Surface albedo feedback in transient climate change over NH extratropical land areas was estimated based on the scenario runs of the current versions of two state-of-the-art climate models, GFDL CM2.0 and NCAR CCSM3.0. According to the classic climate sensitivity framework, the strength of snow albedo feedback is determined by the product of two terms, one representing the change in surface albedo induced by a unit temperature change ($\Delta\alpha_s/\Delta T_s$), and another representing the dependence of planetary albedo on surface albedo ($\partial\alpha_p/\partial\alpha_s$). Although the amplitudes of the surface albedo reduction ($\Delta\alpha_s$) from the current springtime climate to the climate of the end of the 21st century are quite different in the two models, they have the same sensitivity to surface air temperature change (ΔT_s) between the two climate in the two models. The different surface albedo reductions in the two models is because the overall warming is different. This in turn is due to the different strength of other climate feedbacks in the models, most likely global cloud feedback.

The effect of the surface albedo reduction on planetary albedo ($\partial\alpha_p/\partial\alpha_s$) was also examined based on the same simulations. However, our ability to assess this aspect

of snow albedo feedback is constrained by the accompanying changes in cloud cover and cloud optical thickness simulated in CM2.0 and CCSM3.0 which differ not only in amplitude, but also in sign. The disparity in changes in cloud fields between the two models is consistent with the wide divergence in simulations of cloud feedback among current climate models. This makes it difficult to compare the strength of snow albedo feedback processes in climate models in isolation from cloud feedback.

To isolate the surface contribution from that of cloud, we develop an analytical model governing planetary albedo. This model relates full-sky planetary albedo to known quantities, including clear-sky planetary albedo, cloud cover, cloud optical thickness and surface albedo. It captures extremely well both interannual and geographical variability in planetary albedo in simulated and satellite-based data sets. The advantage of this model is that we can use it to derive an expression for partial derivative of planetary albedo with respect to surface albedo, a quantity representing the attenuation effect of the atmosphere on the surface's contribution to planetary albedo fluctuation. It includes a contribution from the cloudless atmosphere, represented by an effective clear-sky atmospheric transmissivity as well as a contribution from cloud, being proportional to the product of cloud cover and logarithm of cloud optical thickness.

There is good agreement in values of the clear-sky component of the atmosphere's attenuation of surface albedo anomalies, both in the current climate among ISCCP, CM2.0, and CCSM3.0, and in the future climate between CM2.0 and CCSM3.0 in both North America and Eurasia, all being about 0.7. Values of the cloud contribution to the variation in planetary albedo with surface albedo are about 1/3 the size of clear sky component. Cloud is not the most significant factor controlling the variation in

planetary albedo with surface albedo both because a substantial fraction of the sky is clear in NH snow-covered regions, and because the atmosphere plays some role in attenuating surface albedo anomalies even when the sky is cloudy. Therefore differences or errors in mean cloud fields of the magnitude seen in the current generation of climate models are not large enough to cause appreciable divergence or errors in estimates of the variation of planetary albedo with surface albedo in the current climate. For example, differences in values of the cloud contribution to the atmospheric attenuation effect among the three data sets in the current climate are generally smaller than 10% of the total attenuation effect. Nor are changes in mean cloud fields as a result of climate change large enough to cause the variation of planetary albedo with surface albedo to exhibit significant time dependence. Because of this relative insensitivity to variations in mean cloud fields, the mean values of the variation of planetary albedo with surface albedo seen in ISCCP, CM2.0, and CCSM3.0 in the current and future climate are in general agreement, all being 0.5. Therefore we can say with a high degree of confidence that both in simulations and satellite-based data sets, snow-induced planetary albedo anomalies are about half the albedo signature at the surface.

Using our analytical model and values of the variation in planetary albedo with surface albedo, we examine the effect of the accompanying cloud changes in the future climate on the planetary albedo variations. We found that they contribute differently to planetary albedo variations in the two models. Nearly all the planetary albedo reduction seen in CM2.0 stems from the surface albedo reduction in both North America and Eurasia, implying that magnitudes of the cloud contributions are small. This is mostly because a decrease of cloud cover is compensated by an increase in cloud optical

thickness. Likewise, clouds in CCSM3.0 do not contribute much to planetary albedo change in Eurasia. However, in North America, the increase in the planetary albedo due to the increase in cloud cover and cloud optical thickness partly cancels the effect of the surface albedo reduction, so that the final planetary albedo reduction is only a third of what it would be if there were no cloud feedback. This suggests the divergence of simulated cloud feedback is most likely a major reason the values of $\Delta\alpha_p/\Delta\alpha_s$ diverge significantly among climate models in the previous estimates of snow albedo feedback.

Our study shows both quantities governing the strength of snow albedo feedback, $\Delta\alpha_s/\Delta T_s$ and $\partial\alpha_p/\partial\alpha_s$ simulated in CM2.0 are about the same as those simulated in CCSM3.0, thus implying the snow albedo feedback in the two models has about the same strength. This may be an indication of convergence in simulations of snow albedo feedback in the new versions of climate models, although more models need to be included in this comparison study. These analyses are currently underway.

Acknowledgments. This study is based on model integrations performed by NCAR and CRIEPI with support and facilities provided by NSF, DOE, ESC/JAMSTEC and MEXT. It was supported by NSF Grant ATM-0135136. The authors wish to thank Y.-C. Zhang for his help with the ISCCP cloud and flux datasets.

References

Briegleb, B. P. and coauthors, 2004: Scientific Description of the Sea Ice Component in the Community Climate System Model, Version Three. NCAR/TN-463+STR, NCAR TECHNICAL NOTE.

Cess, R. D. and coauthors, 1991: Interpretation of snow-climate feedback as produced by 17 general circulation models. *Science*, **253**, 888–892.

Cess, R. D. and G. L. Potter, 1988: A methodology for understanding and intercomparing atmospheric climate feedback processes in general circulation models. *J. Geophys. Res.*, **93**(D7), 8305–8314.

Collins, W. D. and coauthors, 2004: Description of the NCAR Community Atmosphere Model (CAM3.0). NCAR/TN-464+STR, NCAR TECHNOCAL NOTE.

Cubasch, U. and coauthors, 2001: Projections of future climate change. *Climate Change 2001:The Scientific Basis.* Cambridge University Press, pp. 525–582.

GAMDT, 2005: The new GFDL global atmosphere and land model AM2/CM2.0: Evaluation with prescribed sst simulations. Submitted to *J. Climate*.

Groisman, P. Y., T. R. Karl and R. W. Knight, 1994a: Observed impact of snow cover on the heat balance and the rise of continental spring temperatures. *Science*, **263**, 198–200.

Groisman, P. Y., T. R. Karl and R. W. Knight, 1994b: Changes of snow cover, tem-

peratures, and radiative heat balance over the northern hemisphere. *J. Climate*, **7**, 1633–1656.

Hall, A., 2004: The role of surface albedo feedback in climate. *J. Climate*, **17**, 1550–1568.

Holland, M. M. and C. M. Bitz, 2003: Polar amplification of climate change in coupled models. *Climate Dyn.*, **21**, 221–232.

Milly, P. C. D. and A. B. Shmakin, 2002: Global modeling of land water and energy balances. Part I: The land dynamics (LaD) model. *J. Hydrometeorology*, **3**(3), 283–299.

Oleson, K. W. and coauthors, 2004: Techical Description of the Community Land Model (CLM). NCAR/TN-464+STR, NCAR TECHNOCAL NOTE.

Randall, D. A. and coauthors, 1994: Analysis of snow feedbacks in 14 general circulation models. *J. Geophys. Res.*, **99**(D10), 20757–20772.

Rossow, W. B. and L. C. Garder, 1993a: Cloud detction using satellite measurements of infrared and visible radiances for ISCCP. *J. Climate*, **6**, 2341–2369.

Rossow, W. B. and L. C. Garder, 1993b: Validation of ISCCP cloud detections. *J. Climate*, **6**, 2370–2393.

Rossow, W. B. and R. A. Schiffer, 1991: ISCCP cloud data products. *Bull. Amer. Meteor. Soc.*, **72**(1), 2–20.

Rossow, W. B. and R. A. Schiffer, 1999: Advances in understanding clouds from ISCCP. *Bull. Amer. Meteor. Soc.*, **80**(11), 2261–2287.

Rossow, W. B., A. W. Walker, D. Beuschel and M. Roiter, 1996: International Satillite Cloud Climatological Project (ISCCP) description of new cloud datasets. WMO/TD 737, World Climate Research Programme (ICSU AND WMO), 115 pp.

Rossow, W. B., A. W. Walker and L. C. Garder, 1993: Comparison of ISCCP and other cloud amounts. *J. Climate*, **6**, 2394–2418.

Smith, R. and P. Gent, 2004: Reference Manual for the Parallel Ocean Program POP: Ocean System Model CCSM2.0 AND 3.0. LAUR-02-2484.

Zhang, Y.-C., W. B. Rossow, A. A. Lacis, V. Oinas and M. M. Mishchenko, 2004: Calculation of radiative flux profiles from the surface to top-of-atmosphere based on ISCCP and other global datasets: Refinements of the radiative transfer model and the input data. Submitted to *J. Geophys. Res.*

Table and Figure captions:

Table 1: First row: The changes in climatological springtime-mean surface albedo (the first column), surface air temperature (the second column) averaged over North America from the current climate, 1984-2000 to the future warmer climate, 2080-2096 and the ratio of the former to the latter (the third column) in CM2.0. Second row: As in the first row, except for Eurasia. Third row: As in the first row, except for CCSM3.0 data sets. Fourth row: As in the second row, except for CCSM3.0 data sets.

Table 2: First row: The climatological springtime-mean values of ε_2 (the first column), $c \cdot ln(\tau + 1)$ (the second column) over extratropical North America seen in ISCCP in the current climate. Second row: As in the first column, except for extratropical Eurasia. Third row: The climatological springtime-mean values of ε_2 (the first column), $c \cdot ln(\tau+1)$ (the second column) in the current climate and $c \cdot ln(\tau+1)$ (the third column) in the future climate in CM2.0 over extratropical North America. Fourth row: As in the third row, except for extratropical Eurasia. Fifth row: As in the third row, except for CCSM3.0 data sets. Sixth row: As in the fourth row, except for CCSM3.0 data sets.

Figure 1: The geographical distribution of changes in climatological springtime-mean surface albedo (α_s), cloud cover (c), logarithm of cloud optical thickness ($ln(\tau + 1)$) and planetary albedo (α_p) from the current climate (1984-2000) to the future warmer climate (2080-2096) in CM2.0 and CCSM3.0 scenario runs. Here, the changes in surface albedo, cloud cover and planetary albedo are all evaluated by percentage points, rather than a fractional change. Note that surface albedo, cloud cover and planetary albedo are in the units of %, while logarithm of cloud optical thickness is in units of tenths.

The same unit for each variable is also used in Figs 2.

Figure 2: Changes in climatological springtime-mean surface albedo (α_s), cloud cover (c), logarithm of cloud optical thickness ($ln(\tau+1)$) and planetary albedo (α_p) averaged over extratropical North America and Eurasia from the current climate (1984-2000) to the future climate (2080-2096) in CM2.0 and CCSM3.0. In the calculations, changes in the climatological springtime-mean values of α_s, c and $ln(\tau+1)$ and α_p, as shown in Fig 1, were weighted by climatological incoming solar radiation at the surface in the current climate. This technique was used in all calculations involving spatial averages of α_s, c, $ln(\tau+1)$ and α_p in this article. Note that extratropical North America is North America land area northward of 30^0N, including Greenland, and extratropical Eurasia is Eurasian land area northward of 30^0N. Extratropical North America and Eurasia are represented by "NA" and "EU" signs, respectively. These are also used in Figs 7 and 8.

Figure 3: Scatter plots of modeled interannual and geographical variations in springtime-mean planetary albedo based on eq. (10) and interannual and geographical variations in springtime-mean planetary albedo seen in ISCCP, CM2.0 and CCSM3.0 in extratropical North America and Eurasia for the current climate (1984-2000). For clarity, we only show 10% of samples which are randomly chose on each scatter plot. The same technique are also used in Figs 4-6.

Figure 4: Scatter plots of modeled interannual and geographical variations in springtime-mean planetary albedo based on eq. (10) and interannual and geographical variations in springtime-mean planetary albedo seen in CM2.0 and CCSM3.0 in extratropical North America and Eurasia for the future warmer climate (2080-2096).

Figure 5: Scatter plots of modeled interannual and geographical variations in springtime-mean clear-sky planetary albedo and interannual and geographical variations in springtime-mean clear-sky planetary albedo seen in ISCCP, CM2.0 and CCSM3.0 in extratropical North America and Eurasia for the current climate (1984-2000).

Figure 6: Scatter plots of modeled interannual and geographical variations in springtime-mean clear-sky planetary albedo and interannual and geographical variations in springtime-mean clear-sky planetary albedo seen in CM2.0 and CCSM3.0 in extratropical North America and Eurasia for the future warmer climate (2080-2096).

Figure 7: The climatological springtime-mean values of T_a^{cr}, $\varepsilon_2 \cdot c \cdot ln(\tau+1)$ and $\partial\alpha_p/\partial\alpha_s$ seen in ISCCP, CM2.0 and CCSM3.0 in extratropical North America and Eurasia in the current climate (1984-2000) and the future climate (2080-2096). First, regression calculations are performed to obtain values of T_a^{cr}, ε_1 and ε_2 based on eqs. (5) and (10) (see Sections 4 and 5). Then, climatological springtime-mean values of $\varepsilon_2 \cdot c \cdot ln(\tau + 1)$ are calculated at all locations within extratropical North America and Eurasia. Finally, these values are averaged over extratropical North America and Eurasia, respectively. Note that $\partial\alpha_p/\partial\alpha_s = T_a^{cr} + \varepsilon_2 \cdot c \cdot ln(\tau + 1)$.

Figure 8: The breakdown of the climatological springtime-mean values of normalized planetary albedo reduction ($\Delta\alpha_p/\Delta\alpha_s$) in extratropical North America and Eurasia in the future climate (2080-2096) into surface contribution ($\partial\alpha_p/\partial\alpha_s$) and cloud contribution ($\Delta\alpha_p/\Delta\alpha_s - \partial\alpha_p/\partial\alpha_s$), based on eq. (14).

Table 1:

	Regions	$\Delta\alpha_s$	ΔT_s	$\Delta\alpha_s/\Delta T_s$
CM2.0	N. A.	-5.96	4.15	-1.44
	Eurasia	-5.32	4.55	-1.17
CCSM3.0	N. A.	-4.08	2.78	-1.47
	Eurasia	-3.32	2.85	-1.17

Table 2:

	Regions	ε_2	$c \cdot ln(\tau + 1)$ (1984-2000)	$c \cdot ln(\tau + 1)$ (2080-2096)
ISCCP	N. A.	0.16	1.51	—
	Eurasia	0.16	1.34	—
CM2.0	N. A.	0.11	1.72	1.93
	Eurasia	0.10	1.74	1.86
CCSM3.0	N. A.	0.16	1.66	1.81
	Eurasia	0.16	1.64	1.69

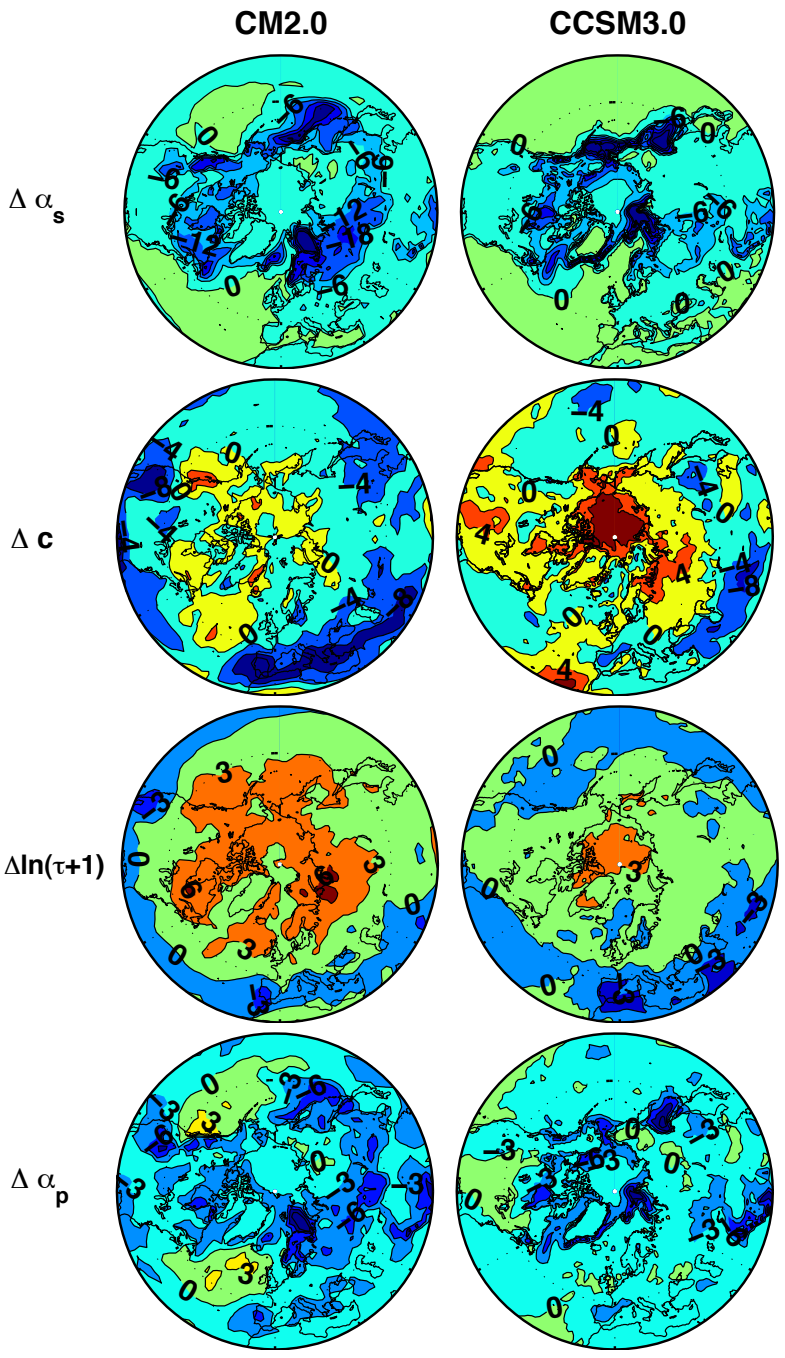

Figure 1:

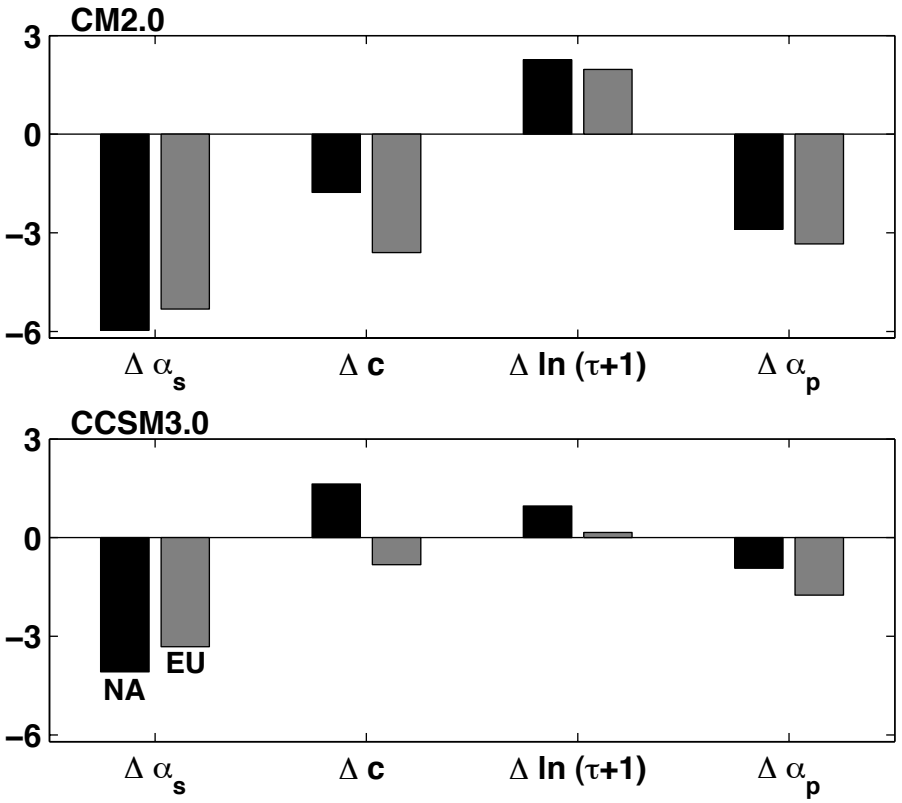

Figure 2:

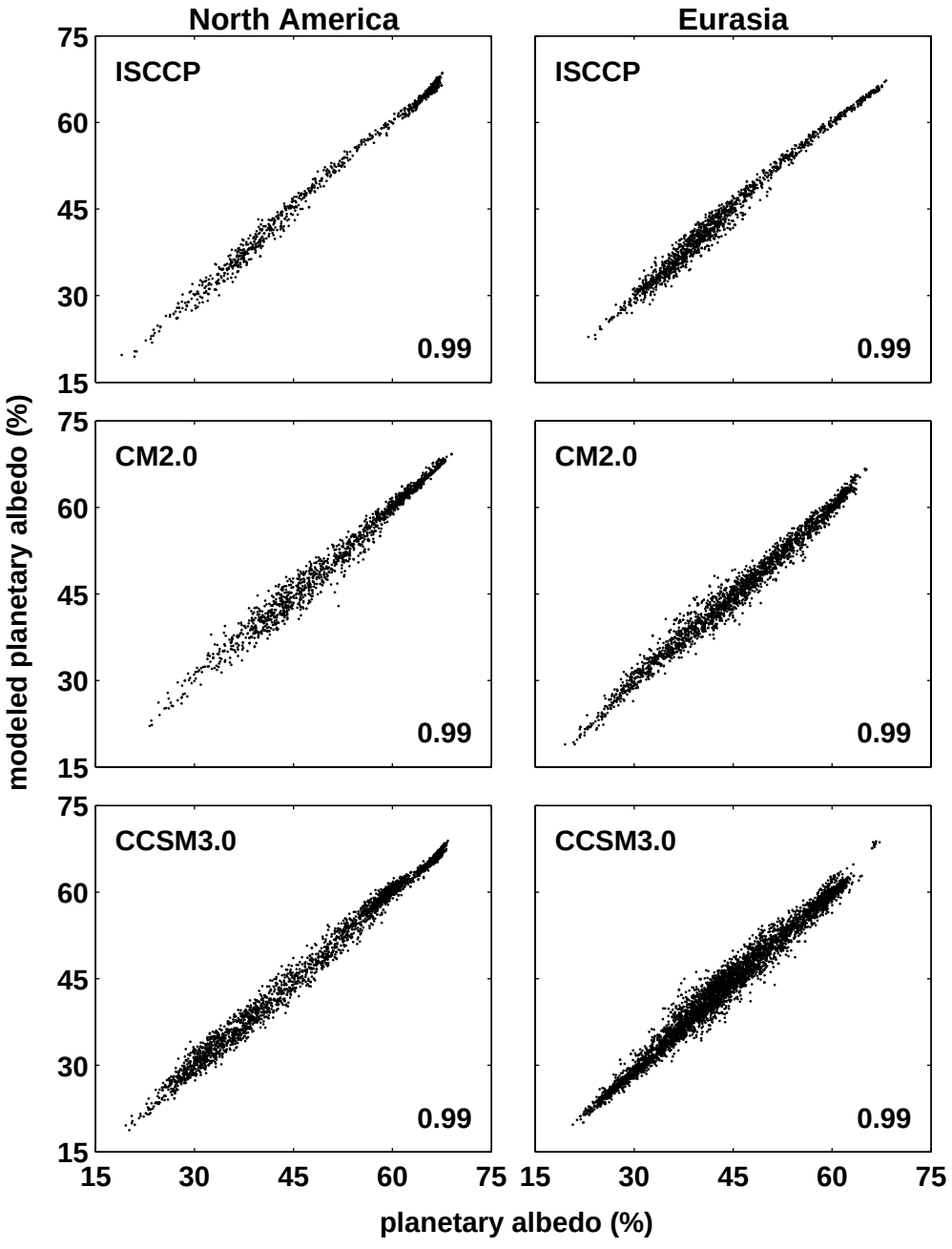
North America
Eurasia
ISCCP
ISCCP
CM2.0
CM2.0
CCSM3.0
CCSM3.0
0.99
0.99
0.99
0.99
0.99
0.99
75
60
45
30
15
15
30
45
60
75
modeled planetary albedo (%)
planetary albedo (%)

Figure 3:

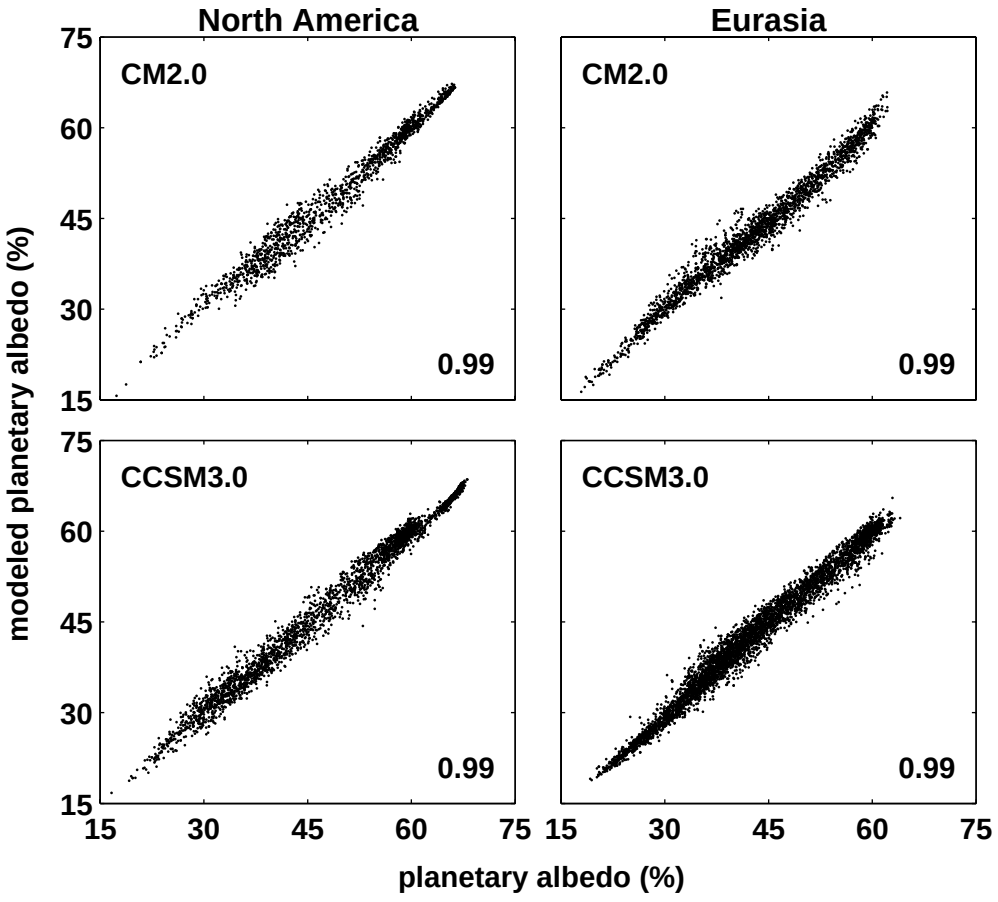
North America
Eurasia
CM2.0
CM2.0
CCSM3.0
CCSM3.0
0.99
0.99
0.99
0.99
modeled planetary albedo (%)
planetary albedo (%)
15
30
45
60
75

Figure 4:

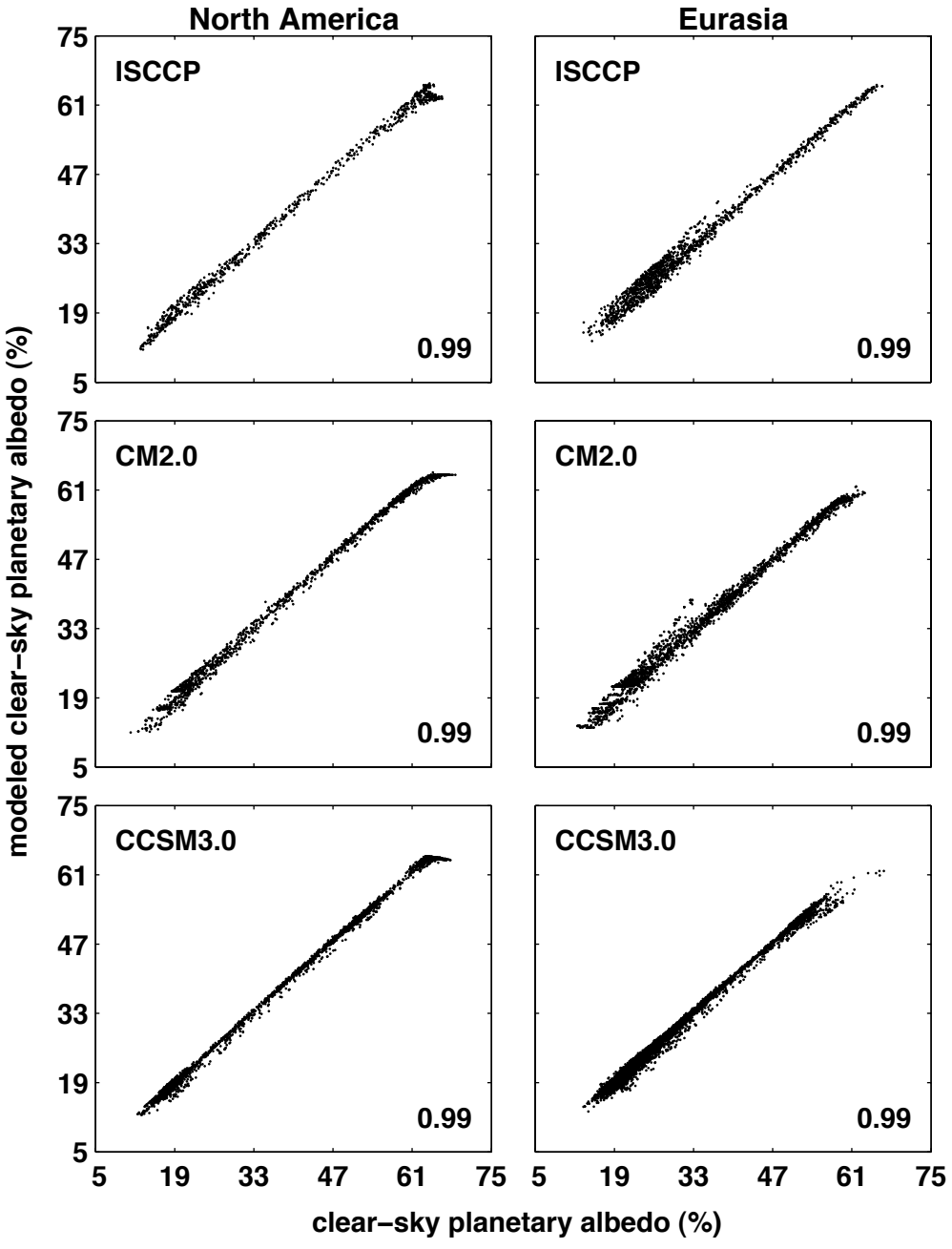
North America
Eurasia
ISCCP
ISCCP
CM2.0
CM2.0
CCSM3.0
CCSM3.0
0.99
0.99
0.99
0.99
0.99
0.99
5
19
33
47
61
75
modeled clear−sky planetary albedo (%)
clear−sky planetary albedo (%)

Figure 5:

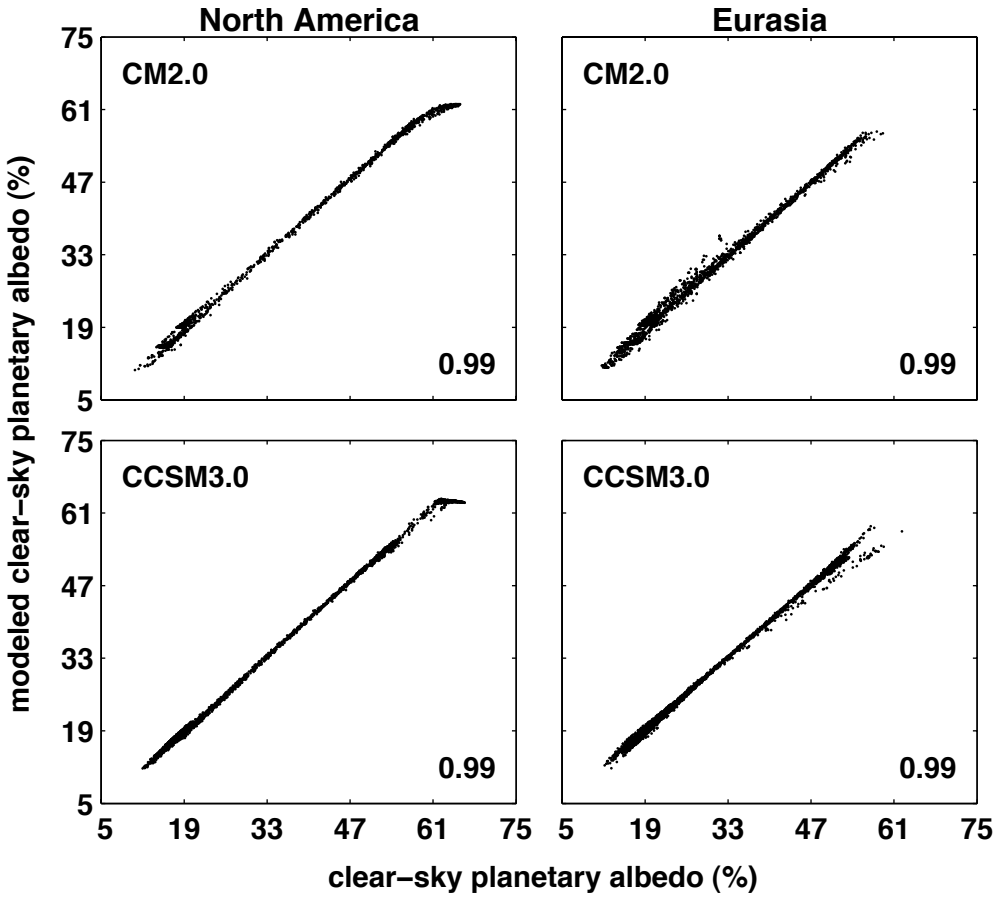
North America
Eurasia
CM2.0
CM2.0
CCSM3.0
CCSM3.0
0.99
0.99
0.99
0.99
75
61
47
33
19
5
modeled clear−sky planetary albedo (%)
clear−sky planetary albedo (%)

Figure 6:

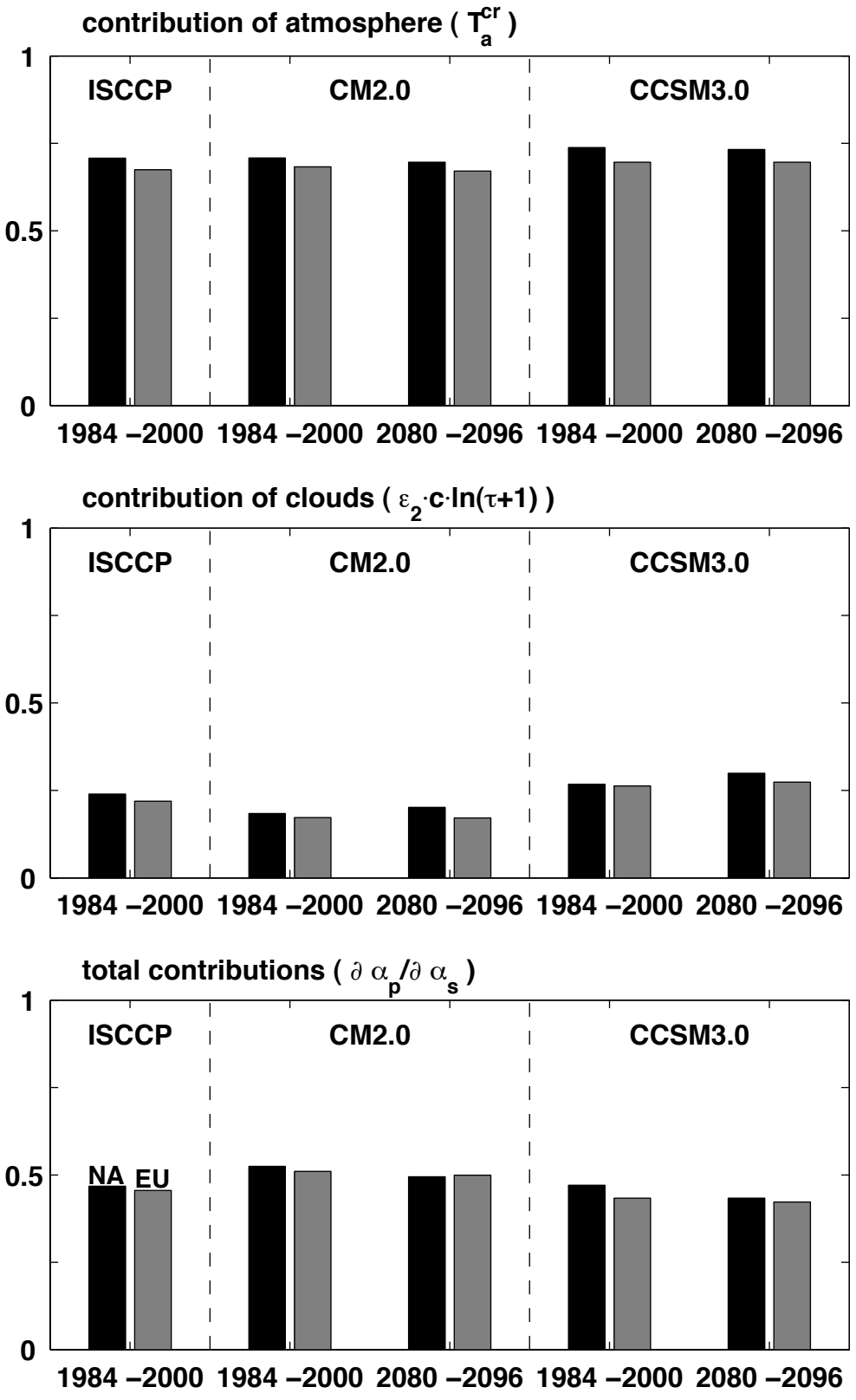
contribution of atmosphere (T_a^{cr})
1
0.5
0
ISCCP
CM2.0
CCSM3.0
1984 –2000
1984 –2000
2080 –2096
1984 –2000
2080 –2096
contribution of clouds ($\varepsilon_2 \cdot c \cdot \ln(\tau+1)$)
1
0.5
0
ISCCP
CM2.0
CCSM3.0
1984 –2000
1984 –2000
2080 –2096
1984 –2000
2080 –2096
total contributions ($\partial \alpha_p / \partial \alpha_s$)
1
0.5
0
ISCCP
CM2.0
CCSM3.0
NA
EU
1984 –2000
1984 –2000
2080 –2096
1984 –2000
2080 –2096

Figure 7:

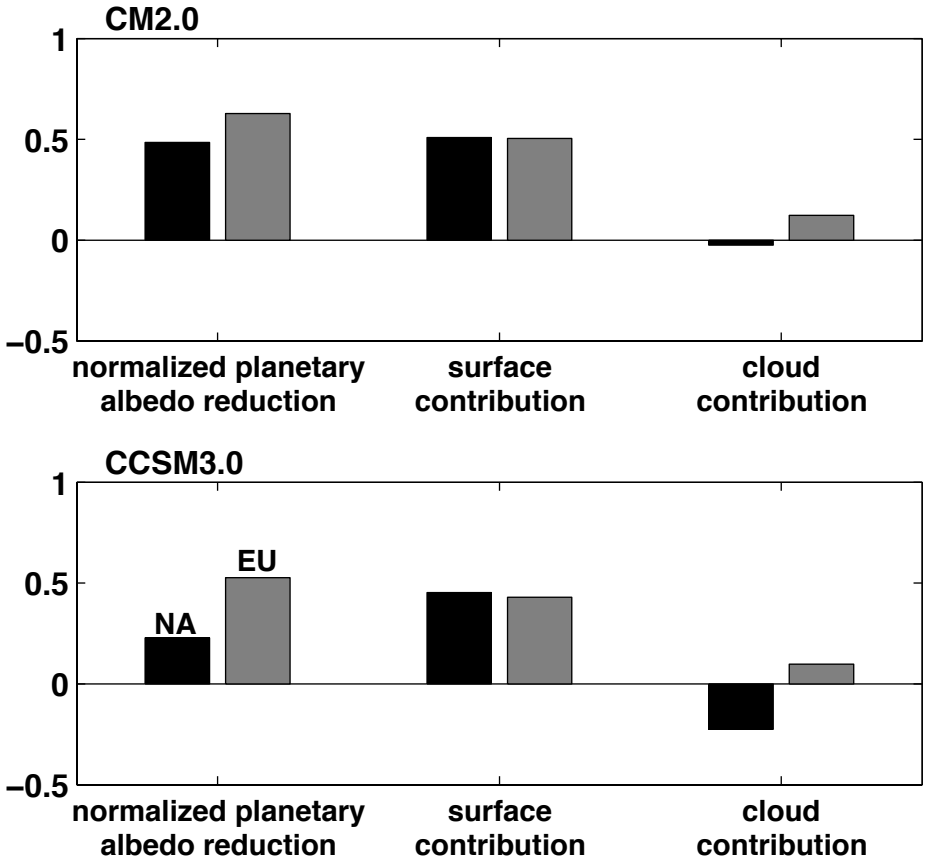
CM2.0
1
0.5
0
−0.5
normalized planetary albedo reduction
surface contribution
cloud contribution
CCSM3.0
1
0.5
0
−0.5
NA
EU
normalized planetary albedo reduction
surface contribution
cloud contribution

Figure 8: